Multi-Cycle-Consistent Adversarial Networks for Edge Denoising of Computed Tomography Images

XIAOWE XU and JIAWEI ZHANG, Guangdong Academy of Medical Sciences
JINGLAN LIU, YUKUN DING, and TIANCHEN WANG, University of Notre Dame
HAILONG QIU, HAIYUN YUAN, JIAN ZHUANG, and WEN XIE, Guangdong Academy of Medical Sciences
YUHAO DONG, QIANJUN JIA, and MEIPING HUANG, Guangdong Academy of Medical Sciences
YIYU SHI, University of Notre Dame

As one of the most commonly ordered imaging tests, the computed tomography (CT) scan comes with inevitable radiation exposure that increases cancer risk to patients. However, CT image quality is directly related to radiation dose, and thus it is desirable to obtain high-quality CT images with as little dose as possible. CT image denoising tries to obtain high-dose-like high-quality CT images (domain Y) from low dose low-quality CT images (domain X), which can be treated as an image-to-image translation task where the goal is to learn the transform between a source domain X (noisy images) and a target domain Y (clean images). Recently, the cycle-consistent adversarial denoising network (CCADN) has achieved state-of-the-art results by enforcing cycle-consistent loss without the need of paired training data, since the paired data is hard to collect due to patients' interests and cardiac motion. However, out of concerns on patients' privacy and data security, protocols typically require clinics to perform medical image processing tasks including CT image denoising locally (i.e., edge denoising). Therefore, the network models need to achieve high performance under various computation resource constraints including memory and performance. Our detailed analysis of CCADN raises a number of interesting questions that point to potential ways to further improve its

Xiaowe Xu, Jinglan Liu, and Hailong Qiu contributed equally to this research.

This work was supported by the National Key Research and Development Program of China (2018YFC1002600), the Science and Technology Planning Project of Guangdong Province, China (2017B090904034, 2017B030314109, 2018B090944002, 2019B020230003), Guangdong Peak Project (DFJH201802), and the National Natural Science Foundatio of China (62006050).

Authors' addresses: X. Xu and J. Zhang, Guangdong Cardiovascular Institute, Guangdong Provincial Key Laboratory of South China Structural Heart Disease, Guangdong Provincial People's Hospital, Guangdong Academy of Medical Sciences, 106 Zhongshan Second Road, Guangzhou, Guangdong, 510080; emails: xuxiaowei@gdph.org.cn, 17110240008@fudan.edu.cn; J. Liu, Y. Ding, T. Wang, and Y. Shi, Department of Computer Science and Engneering, University of Notre Dame, Notre Dame, IN 46556; emails: {jliu16, yshi4}@nd.edu; H. Qiu, H. Yuan, J. Zhuang, and W. Xie (corresponding author), Department of Cardiovascular Surgery, Guangdong Cardiovascular Institute, Guangdong Provincial Key Laboratory of South China Structural Heart Disease, Guangdong Provincial People's Hospital, Guangdong Academy of Medical Sciences, 106 Zhongshan Second Road, Guangzhou, Guangdong, 510080; emails: hailong0518@qq.com, yhy_yun@163.com, Zhuangjian5413@163.com, Xiewen0231@qq.com; Y. Dong, Q. Jia (corresponding author), and M. Huang (corresponding author), Department of Catheterization Lab, Guangdong Cardiovascular Institute, Guangdong Provincial Key Laboratory of South China Structural Heart Disease, Guangdong Provincial People's Hospital, Guangdong Academy of Medical Sciences, 106 Zhongshan Second Road, Guangzhou, Guangdong, 510080; emails: barbaradong1@outlook.com, jiaqianjun@126.com, huangmeiping@126.com.

1550-4832/2021/07-ART58 $15.00
https://doi.org/10.1145/3462328

performance using the same or even fewer computation resources. For example, if the noise is large leading to a significant difference between domain X and domain Y, can we bridge X and Y with a intermediate domain Z such that both the denoising process between X and Z and that between Z and Y are easier to learn? As such intermediate domains lead to multiple cycles, how do we best enforce cycle- consistency? Driven by these questions, we propose a multi-cycle-consistent adversarial network (MCCAN) that builds intermediate domains and enforces both local and global cycle-consistency for edge denoising of CT images. The global cycle-consistency couples all generators together to model the whole denoising process, whereas the local cycle-consistency imposes effective supervision on the process between adjacent domains. Experiments show that both local and global cycle-consistency are important for the success of MCCAN, which outperforms CCADN in terms of denoising quality with slightly less computation resource consumption.

CCS Concepts: • **Computing methodologies** → *Image representations*; • **Hardware** → *Emerging tools and methodologies;*

Additional Key Words and Phrases: Adversarial network, computed tomography, deep learning, image denoising, image translation

ACM Reference format:
Xiaowe Xu, Jiawei Zhang, Jinglan Liu, Yukun Ding, Tianchen Wang, Hailong Qiu, Haiyun Yuan, Jian Zhuang, Wen Xie, Yuhao Dong, Qianjun Jia, Meiping Huang, and Yiyu Shi. 2021. Multi-Cycle-Consistent Adversarial Networks for Edge Denoising of Computed Tomography Images. *J. Emerg. Technol. Comput. Syst.* 17, 4, Article 58 (July 2021), 16 pages.
https://doi.org/10.1145/3462328

1 INTRODUCTION

The privacy and security of patient data have always been the primary concern in medical applications among hospitals and clinics. As such, protocols typically require medical image processing tasks such as denoising [3, 24, 28, 34], segmentation [18, 27, 31, 32, 37–39], and diagnosis [33] to be performed locally (i.e., on the edge). However, local machines and devices are usually with rather limited computation resources including memory capacity and performance compared with those in the cloud. The constrained resources can have profound impact on the design of medical image processing algorithms. In this article, we will use **computed tomography (CT)** image denoising as a vehicle to demonstrate it.

CT is one of the most widely used medical imaging modalities for showing anatomical structures [36]. The foremost concern of CT examination is the associated exposure to radiation, which is known to increase the lifetime risk for death from cancer [8]. The radiation dose can be lowered at the cost of increased noise [14, 36]. Such noise in a CT image leads to both degraded perceptual quality and degraded diagnostic confidence of a doctor. A general principle in dose management in practice is "as low as reasonably achievable" [20]. Thus the resulting images are denoised for minimized the loss on perceptual quality and diagnostic confidence of radiologists. Even with tremendous effort and significant progresses in the past few decades, the radiation exposure of CT scan was still estimated to account for up to 2% of cancer incidence in the United States [25].

Various deep neural network based methods exist for CT image denoising [3, 24, 28, 34], which require paired clean and noisy images for training. Yet paired images are hard to collect due to patients' interests and cardiac motion. Therefore, simulations are usually used to generate such paired data, where the simulated noise patterns can be different from the real ones, leading to biased training results [11]. To address this issue, recently the **cycle-consistent adversarial denoising network (CCADN)** was proposed by Anoosheh et al. [11], which formulates CT image denoising as an image-to-image translation problem without paired training data. CCADN consists of two generators: one transforms noisy CT images (domain X) to clean ones (domain Y), and

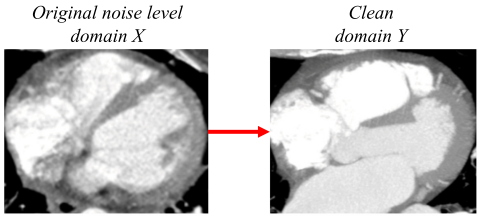

(a) Two domains in CCADN with a single step

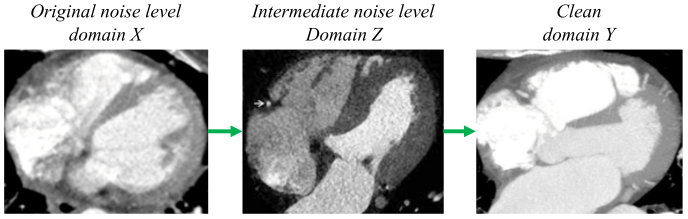

(b) Three domains in the proposed MCCAN with multiple steps

Fig. 1. Comparison of domains in CCADN (a) and the proposed MCCAN (b). CCADN performs single-cycle-consistent adversarial training with two domains, whereas the proposed MCCAN performs multiple-cycle-consistent adversarial training with more than two domains (e.g., three).

the other transforms clean CT images (domain Y) to noisy ones (domain X). Both generators are trained by adversarial loss. In addition, they form a cycle where a noisy CT image can be transformed to a clean one and transformed back to a noisy one (i.e., $X \rightarrow Y \rightarrow X$). Cycle-consistency loss is defined by the difference between the two noisy CT images, which is a key component to controlling the training of both generators for better performance. Cycle-consistency loss is also imposed for $Y \rightarrow X \rightarrow Y$ transform. However, CCADN only works well when the noise levels are low. This is because it only contains two domains X and Y, and therefore its efficacy degrades as the noise becomes stronger, leading to larger differences between X and Y that are harder to learn. A larger neural network with stronger representation power is needed, which may not be feasible with the limited computation resources on the edge.

To enhance the performance of CCADN without increasing the resource consumption, as shown in Figure 1, we propose to establish an intermediate domain between the original noisy image domain X and clean image domain Y, and decompose the denoising task into multiple coupled steps such that each step is easier to learn by deep neural network based models. Specifically, we construct an additional domain Z with images of intermediate noise level between X and Y. These images can be considered as a stepping stone in the denoising process and provide additional information for the training of the denoising network. The multi-step framework particularly suits the denoising problem: although it is difficult to either find or define a good collection of images in the "half-cat, half dog"domain in a "cat-to-dog" type of image translation problems, a domain Z of images with an intermediate level of noise exists naturally. In addition, when the denoising problem (two domains) is divided into several subproblems (N domains), each subproblem is much easier to solve. In this way, the network complexity for each subproblem (e.g., number of parameters) is usually lower than $1/(N-1)$ of the original network [30]. Thus, the overall computation consumption can be reduced.

With the new domain Z, we further propose a **multi-cycle-consistent adversarial network (MCCAN)** to perform the multi-step denoising, which builds multiple cycles of different scales (global cycles and local cycles) between the domains while enforcing the corresponding cycle-consistencies. Specifically, global cycles combine all of the generators and domains together to

model the entire denoising process. The local cycles serve two purposes. First, they impose effective supervision on the generators between adjacent domains. Second, while each step is easier, the multi-step framework leads to deeper networks and makes it challenging for end-to-end training. The local cycles can provide a gradient from the supervised training of easier tasks on shallower networks, thus alleviating the problem. The experimental results show that both global cycles and local cycles are necessary, and our method MCCAN outperforms the state-of-the-art competitor CCADN with slightly less resource consumption.

2 RELATED WORKS

2.1 CT Image Denoising

Numerous CT image denoising methods can be categorized as three types: signogram filtering-based method, iterative reconstruction, and image space denoising [36]. The first two types of methods are usually embedded within the CT scanner as commercial algorithms, and thus we focus more on the last type of method for research.

The signogram filtering-based method performs in the original projection space before filtered backprojection is applied to reconstruct images [15, 19]. One common advantage of this method is that the noise properties in projection space are fairly well understood. However, the image sharpness may degrade because the edges are not well defined in projection data [14].

Iterative reconstruction is considered the most accurate one by using statistical assumptions about the noise properties in projection space, prior information in image space, and various accurate information of the specific scanner [22]. However, the implementation highly depends on specific scanner models and is very computationally extensive for each scan [14, 29].

Image space denoising is performed on the reconstructed images, and thus the computation cost is much lower than that in the first two categories. In recently years, deep neural networks and various methods developed in other areas are combined with CT image denoising, including GAN, autoencoder, perceptual loss, transfer learning, and 3D convolution [3, 24, 28, 34]. Mostly recently, CycleGAN was applied to CT denoising as CCADN and achieved better results than the state of the art [11].

It can be hard to find a standard metric to measure denoising performance when there are no paired samples for test. For the protection of patients and operators, repetitive CT scanning is usually not permitted due to the additional radiation dose. Even if repetitive scan is available, cardiac motion or the changed operating condition will make two scans different. This problem is alleviated by simulating corresponding low-dose images from high-dose images with noise modeling [6, 12]. However, noise should be added in the sinogram domain in the synthetic CT scan images, which is too difficult to implement without assistance from the CT scanners' vendor [11]. As well, the additional noise pattern can be different from the real noise pattern. This will introduce bias in the data and result in biased denoising models.

2.2 Image-to-Image Translation

Our work is closely related to some of the popular image-to-image translation models using generative adversarial networks [9] or neural style transfer [10]. Image-to-image translation also includes some other artifact removal problems similar to denoising, such as raindrop removal and shadow removal [16, 23, 26]. Wang et al. [26] use a joint-learned two-step approach for shadow removal where one conditional GAN [21] is used to detect the shadow region and the result is used by another conditional GAN for shadow removal. However, these two steps are mostly specific to a small set of problems and cannot be applied to other cases with more steps.

Although the use of cycle consistency loss has achieved significant progress [13, 35, 40], the models still have some drawbacks. CycleGAN often succeeds on translation of low-level features

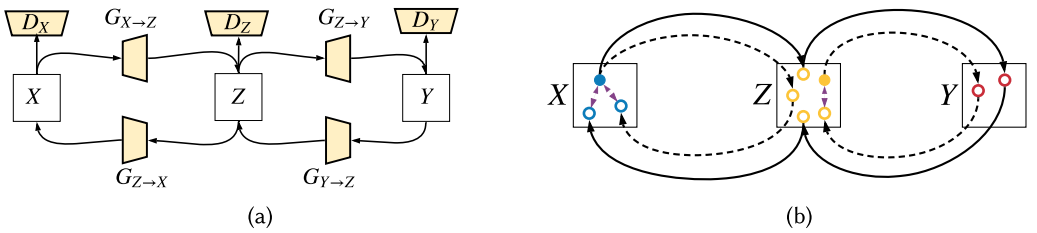

Fig. 2. Structure of MCCAN (a) and its cycles (b). The arrows inside each domain denote the computation of cycle-consistency loss. The solid and dashed arrows across domains form global and local cycles, respectively. For clarity, we only show cycles from left to right. Symmetric cycles going from right to left also exist but are not shown.

including color and texture but has little success on tasks with geometric changes [40]. We anticipate that the multiple-step approach can potentially alleviate this problem. However, CycleGAN can be inefficient for translation in multiple domains, because the number of translation models grows quadratically with the number of domains. Motivated by this, StartGAN and ComboGAN [1, 4] propose new models to get better scalability. The training method of CycleGAN in the facial attribute transfer experiment of Choi et al. [4] is essentially the MCCAN without global cycles. ComboGAN is used to perform multi-step transformation (e.g., changing gender after changing hair color). The results show that image quality degrades with more translation steps. We analyze the possible reason—the lack of global cycles—in Section 3.

Coupled GAN (CoGAN) is proposed by Liu and Tuzel [17] to learn a joint distribution in different domains without paired samples. Based on the assumption that deep neural networks learn a hierarchical feature representation, CoGAN enforces the GANs to decode high-level semantics in the same way by sharing the weights. To translate an image x in domain X to domain Y, it has to find the random vector that generates x through the generator for X and then apply the generator for Y to this random vector. Such a search process could be very time consuming [5]. Another limitation is that the transformation only successful when x is covered by the generator for X (can be generated by this generator). Although it is not discussed in their work, we found that their approach implicitly uses a feature map domain as a bridge for the translation. Specifically, if we assume that the query image is always covered by the corresponding generator, their structure can be considered as building a domain graph in which each image domain is connected to a central feature map domain. When doing the translation, it always translates as $X \to Z \to Y$, where Z is the feature map domain. In this article, we equip MCCAN with available CT images from different domains (radiation dose) directly for the denoising task without increasing resource consumption.

3 MULTI-CYCLE-CONSISTENT ADVERSARIAL NETWORKS

Given training images that are either labeled as noisy (domain X) or clean (domain Y), we first construct a new domain Z that contains images with an intermediate noise level between X and Y. How to obtain Z is flexible in practice. It can either be obtained from X and Y by separating out those images with intermediate noise level, if available, or from images scanned with a medium dose, or from common techniques including injecting an intermediate level of noise to the images in Y.

With CT images from three domains, the multi-step denoising architecture of MCCAN is shown in Figure 2(a). We train four convolutional neural networks as generators and three as discriminators. Arrows in Figure 2(a) define how images are transformed in the training stage. Specifically, the generator $G_{X\to Z}$ aims to transform an image from X to Z. $G_{Z\to X}$, $G_{Z\to Y}$, and

$G_{Y\to Z}$ can be interpreted similarly. Discriminators D_X, D_Y, and D_Z aim to distinguish the "real" images originally belonging to the domains X, Y, and Z, respectively, from the "fake" images transformed from other domains.

As the MCCAN structure in Figure 2(a) contains thee domains, there are multiple ways in which we can construct cycles (paths where an image from a source domain is transformed through one (in the work of Zhu et al. [40]) or several other domains (in this article) and back to the source domain) for cycle-consistent loss. In particular, we introduce two types of cycles as shown in Figure 2(b). In this figure, each dot represents an image, which is color coded based on the domain. The solid ones represent the images originally in the domain ("real" ones), and the hollow ones represent those transformed from another domain ("fake" ones). As such, the dashed arrows form the *local cycles*, each of which goes across only two adjacent domains. However, the solid arrows constitute a *global cycle* that starts from X through Z, Y, Z, and back to X sequentially. Note that in the figure we only show half of the cycles (from left to right) for clarity, and the other half that are from right to left and symmetric to the ones shown also exist. We then enforce cycle-consistency loss, which measures the difference between the original images and the final images produced at the end of the cycle as represented by the small arrows within each domain in Figure 2(b). Ideally, the images transformed back to the source domain should be identical to the original images. The cycle-consistency loss is applied to every cycle, no matter whether it is local or global.

The global cycles are important for the denoising performance for the following reason. In the inference stage, an input noisy CT image x in domain X will be transformed by $G_{X\to Z}$ and $G_{Z\to Y}$ sequentially, which means that $G_{X\to Z}$ and $G_{Z\to Y}$ are coupled by data dependency. Without global cycles, $G_{X\to Z}$ and $G_{Z\to Y}$ will be trained independently. The global cycles enable the joint training of the generators, which models the denoising path used in the inference stage for better consistency.

The local cycles are also important to address two issues in the training. First, the global cycles go through all four generators and have long paths for the gradient to back-propagate, which makes end-to-end optimization difficult. The locals cycles are shallow and have shorter paths for the gradient to back-propagate. Second, adversarial training only enforces the generators to output "fake" images identically distributed as the original "real" images in the intermediate domain Z. However, they do not necessarily preserve the meaningful content in the inputs, which is critical for the denoising task. The local cycle-consistency supervises each generator to learn to transform images while preserving their meaningful content from the inputs more easily.

In summary, our MCCAN has three major advantages over CCADN. First, it decomposes the one-step transform into multiple steps using constructed images in an intermediate domain as a stepping stone. Second, it not only incorporates global cycles that model the denoising path in the inference stage for consistency but also uses local cycles that provide strong supervision to facilitate the more challenging training process. Third, the network structure of generators can be simplified due to the relatively easier task in each transformation, thus potentially reducing memory and computation consumption.

Note that in the discussion so far, only one intermediate domain has been assumed. It is also possible to include more than one intermediate domain with more global and local cycles. However, our study suggests that any additional domains beyond one will not introduce further performance gain in the dataset we explored.

3.1 Network Architectures

We compare MCCAN with a state-of-the-art CT denoising framework: CCADN [11]. To see how the local cycles and global cycles contribute to the final performance, we also implement and compare MCCAN without local cycles and without global cycles, respectively, as an ablation study.

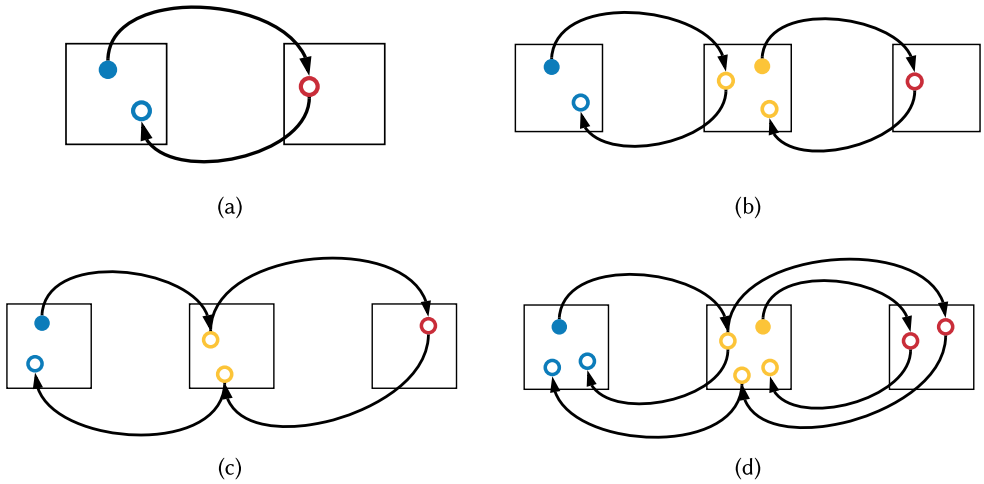

Fig. 3. Comparison of CCADN (a), MCCAN without global cycles (b), MCCAN without local cycles (c), and MCCAN (d). For the clarity of presentation, we only show cycles from left to right, and symmetric cycles from right to left also exist.

The various structures are shown in Figure 3. For the clarity of presentation, only cycles from left to right are shown, but symmetric cycles from right to left also exist.

To ensure that model sizes, computation operations, and number of training epochs are the same for fair comparisons, different network structures are applied in experiments. Generally speaking, all discriminators are used for a same discrimination task in each image domain, so all discriminators share a same network structure. However, generator structures are different for different tasks, since the capability of generators denoising by one step and the capability of generators denoising by more steps, two steps here, are supposed to be different.

Traditional convolution networks are used as the discriminator for all domains in all experiments. In terms of the generators, since there are two types of generators in our experiments, different network architectures are utilized in our experiments. Both network architectures share the same layers for pre-processing and post-processing, as shown in Figure 4. However, the generators transferring images between two domains that are different from each other should have more layers and parameter, and vice versa. So the generators in CCADN are implemented with more residual blocks (ResBlock) as shown in Figure 4(b), whereas generators in MCCAN, MCCAN without local cycles, and MCCAN without global cycles are all implemented as the network architecture shown in Figure 4(a). As a result, the total number of parameters used in each experiment in inference is around 11M to make sure that each method consumes the same memory resources.

3.2 Training Objectives

Finally, we state the training objective used in our framework. Denote $\{G\}$ and $\{D\}$ as the set of generators and discriminators, respectively. Denote $I \in \{X, Y, Z\}$ as one domain and D_I as the discriminator associated with domain I. We let C_i be a cycle and $P_{i,j}$ be a path of half C_i that has the same source domain, where i, j are used merely to distinguish different cycles and paths. For example, $X \rightarrow Z \rightarrow X$ is a cycle, saying C_1, and thus we can have $P_{1,1} = X \rightarrow Z$, and $P_{1,2} = Z \rightarrow X$, which are both half cycles of C_1. $\{P_I\}$ represents the set of all paths that end at domain I. We denote

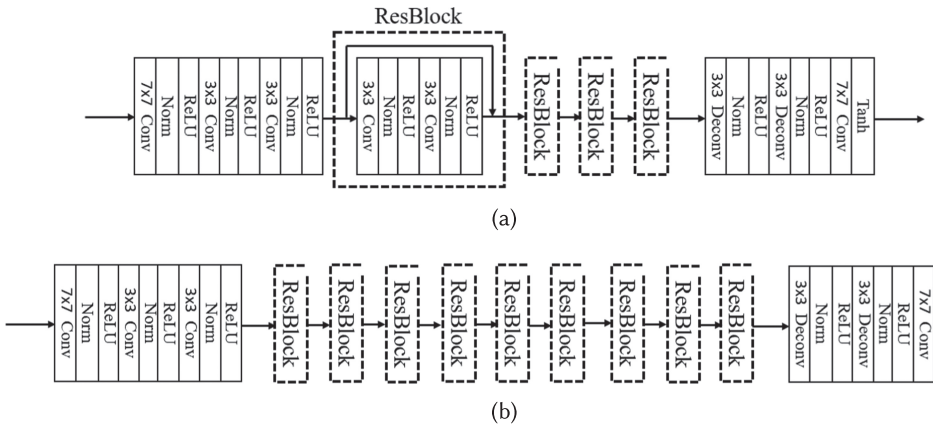

Fig. 4. Network architectures of generators for MCCAN (a) and CCADN (b). ResBlock represents residual blocks [7]. For MCCAN, MCCAN without local cycles, and MCCAN without global cycles, the network architecture in (b) are shared, and these generators only transfer between adjacent domains. Nevertheless, generators in CCADN need to transfer images between more than one domain, thus with larger networks.

I_{C_i} as the source domain of C_i and $G_{P_{i,j}}$ as the ordered function composition of the generators in $P_{i,j}$. Thus, the total adversarial loss is

$$\mathcal{L}_{GAN}(\{G\},\{D\}) = \sum_{I\in\{X,Y,Z\}} \sum_{P_{i,j}\in\{P_I\}} \mathcal{L}_{GAN}(I, P_{i,j}), \tag{1}$$

where $\mathcal{L}_{GAN}(I, P_{i,j})$ is the adversarial loss associated with domain I and the transform path $P_{i,j}$. $\mathcal{L}_{GAN}(I, P_{i,j})$ is obtained by

$$\begin{aligned}\mathcal{L}_{GAN}(I, P_{i,j}) =& \mathbb{E}_{y\sim p_{data}(I)}[\log D_I(y)] \\ &+ \mathbb{E}_{x\sim p_{data}(I_{C_i})}[log(1 - D_I(G_{P_{i,j}}(x)))],\end{aligned} \tag{2}$$

where p_{data} is the distribution of "real" images in a domain and $D_I(x)$ represents the probability determined by D_I that x is a "real" image from domain I rather than a "fake" one transformed by generators from another domain.

The cycle-consistency loss is associated with each C_i, defined as

$$\mathcal{L}_{\text{cyc}}(\{G\}, C_i) = \mathbb{E}_{x\sim p_{\text{data}}(I_{C_i})}[|G_{C_i}(x) - x|_1]. \tag{3}$$

The identity loss is associated with each generator in G, defined as

$$\begin{aligned}\mathcal{L}_{\text{idt}}(\{G\}) = & \sum_{I\in\{X,Y,Z\}} \sum_{J\in\{X,Y,Z\}, J\neq I} \\ & (\mathbb{E}_{x\sim p_{\text{data}}(I)}[|G_{J\to I}(x) - x|_1]).\end{aligned} \tag{4}$$

The final optimization problem we solve in the training stage is

$$\begin{aligned}\{G\}^* = \arg\min_{\{G\}}\max_{\{D\}}(&\mathcal{L}_{GAN}(\{G\},\{D\}) \\ &+ \lambda_{\text{cyc}} \sum_{C_i\in\{C\}} \mathcal{L}_{cyc}(\{G\}, C_i) \\ &+ \lambda_{\text{idt}} \cdot \mathcal{L}_{\text{idt}}(\{G\}),\end{aligned} \tag{5}$$

where λ_{cyc} and λ_{idt} are set to 10 and 0.5, respectively, in our experiments.

Table 1. Comparison of Denoising Performance Between Configurations Using Different Numbers of Domains in MCCAN over the Selected Areas in Figure 5(a)

Method	Mean	SD
Original	1,321.2	84.5
CCADN (two domains) [40]	1,284.1	67.8
MCCAN (three domains)	1,251.4	60.6
MCCAN (four domains)	1,244.1	77.6

4 EXPERIMENTS AND RESULTS

4.1 Experiment Setup

The original dataset contains 200 clean (normal-dose) 3D cardiac CT images and 200 noisy (low-dose) ones from various patients for training, and a separate 11 images for test. The dataset is captured from six patients (three for normal dose and three for low dose). All examinations are performed with a wide detector 256-slice MDCT scanner (Brilliance iCT, Philips Healthcare) providing 8 cm of coverage. Each 2D CT image is of size 512×512, which is then be randomly cropped into 256×256 for data augmentation. We extract the noise pattern from the noisy CT images and add them to the clean CT images with a weighting factor of $\frac{1}{2}$ to generate new CT images with the intermediate noise level.

Following existing works [2, 28, 34], we use the mean and **standard deviation (SD)** of pixels in homogeneous regions of interest chosen by our radiologists to quantitatively judge the quality of CT images. The mean, which reflects substance information, should be as close to that in the original image as possible, and the SD, which reflects noise, should be as low as possible.

We first discuss how the number of domains affects the denoising performance of MCCAN. Then we compare MCCAN with a state-of-the-art CT denoising framework (CCADN [11]), which is also based on cycle-consistency loss but contains only two domains. To see how the local cycles and global cycles contribute to the final performance, we also implement and compare MCCAN without local cycles and without global cycles, respectively, as an ablation study. The various structures are shown in Figure 3. We train all networks following the setting in the work of Zhu et al. [40]. As shown in Figure 5 and Figure 6, six images chosen by our radiologist are used for the qualitative evaluation, and 12 homogeneous areas annotated by red rectangles and numbers are used for quantitative evaluation. All network sizes and numbers of training epochs are the same for fair comparisons.

4.2 Discussion of the Number of Domains

As shown in Table 1, the average mean and SD in five areas indicated in Figure 5(a) are presented. Compared with the original image, CCADN can largely reduce the noises by about 20%. MCCAN with three domains can further improve the image quality with reduced noise by about 8.4%. However, MCCAN with four domains obtains reduced improvement compared with that with three domains and CCADN. Actually, this is expected. More domains require more datasets with different levels of noise, and the difference between the datasets with adjacent levels of noise is smaller. When the difference gets too small, the network can no longer learn it effectively, resulting in degraded performance. For our collected dataset, the optimal number of domains is three, and other datasets may have a different optimal number of domains. How to effectively identify the optimal number of domains for a given dataset can be an interesting problem worth further study.

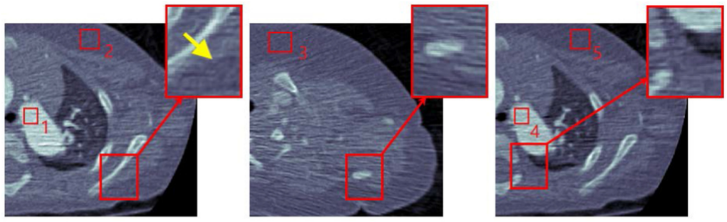

(a) Original noisy CT images

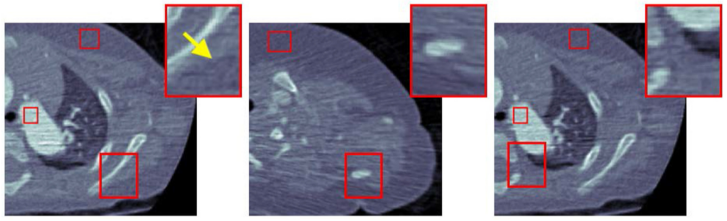

(b) Images denoised by CCADN

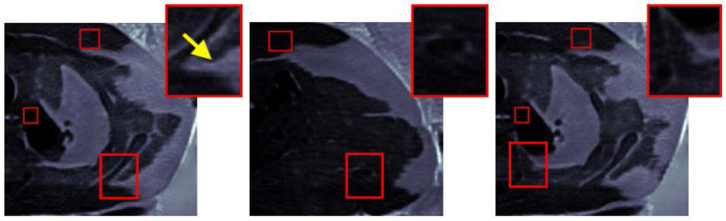

(c) Images denoised by MCCAN without local cycles

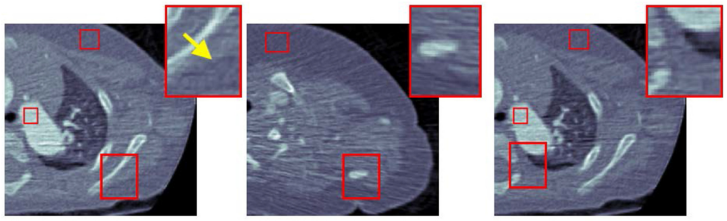

(d) Images denoised by MCCAN without global cycles

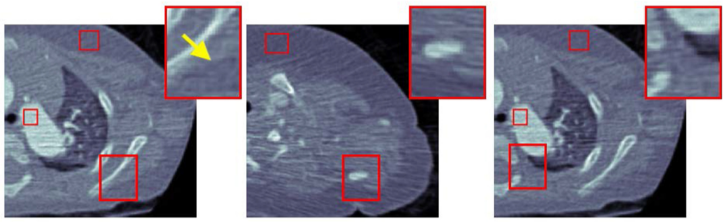

(e) Images denoised by MCCAN

Fig. 5. (a) Original noisy CT images and the corresponding ones denoised by (b) CCADN [11], (c) MCCAN without local cycles, (d) MCCAN without global cycles, and (e) MCCAN. (Best viewed in color.)

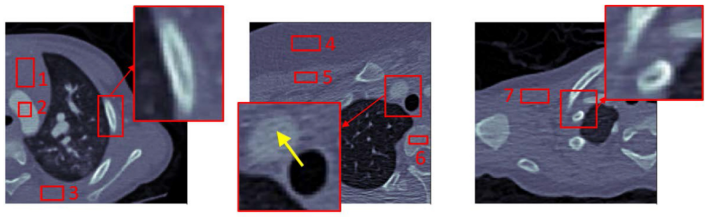

(a) Original noisy CT images

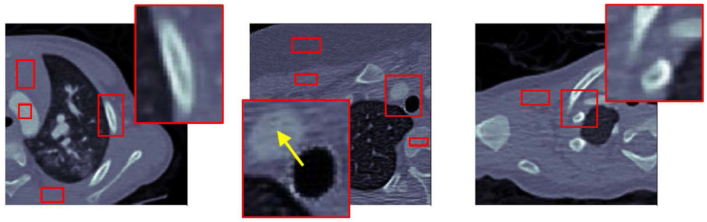

(b) Images denoised by CCADN

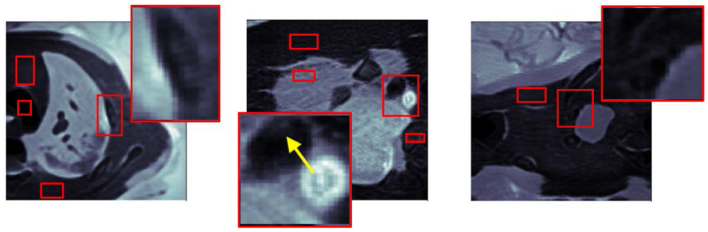

(c) Images denoised by MCCAN without local cycles

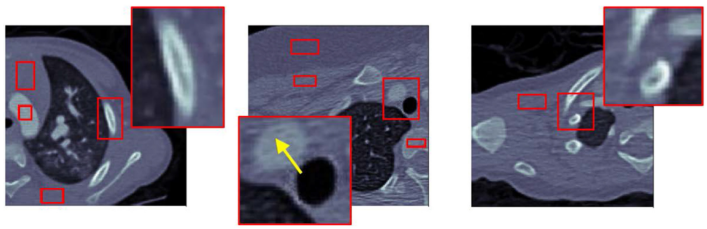

(d) Images denoised by MCCAN without global cycles

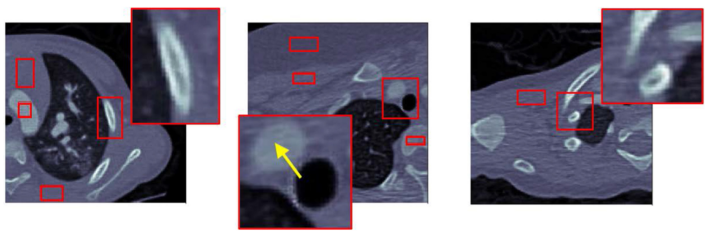

(e) Images denoised by MCCAN

Fig. 6. (a) Original noisy CT images and the corresponding ones denoised by (b) CCADN [11], (c) MCCAN without local cycles, (d) MCCAN without global cycles, and (e) MCCAN. (Best viewed in color.)

Table 2. Comparison of the Number of Parameters (Memory) and Operations (Computation) Between the Proposed Method and the State-of-the-Art CCADN for Inference

Method	Parameters (#)	FLOPs
CCADN [40]	11.4M	745G
MCCAN w/o local cycles	11.0M	668G
MCCAN w/o global cycles	11.0M	668G
MCCAN	11.0M	668G

Note: There is one generator in CCADN, whereas there are two in MCCAN. FLOP stands for floating point operation.

4.3 Comparison with the State-of-the-Art Method

4.3.1 Comparison of Resource Consumption. Comparison of the number of parameters and floating point operations between the proposed method and the state-of-the-art CCADN in inference is shown in Table 2. We can notice that the number of parameters and operations of MMCAN is slightly less than that of CCADN, and MCCANs with different configurations have the same number of parameters and operations. This is because there are two generators with the same network structure in inference for MCCANs with different configurations. Note that although MCCAN without global cycles is supposed to have the same network architecture as MCCAN, there is one extra discriminator associated with the intermediate domain Z. The reason for the extra discriminator is that if there is only one discriminator associated with domain Z, the information from both domain X and domain Y will help it to learn, which results in a stronger discriminator than a discriminator with only one local cycle. In other words, information from the global scope, both domain X and domain Y here, converges at the discriminator. Then the information would be propagated to generators connected with the discriminator as well as whole networks. This is what we would not want to see. Thus, two discriminators are utilized, as well as one for each local cycle to break the global information communication.

4.3.2 Qualitative Evaluation. We chose six representative low-dose CT images in the test dataset as shown in Figure 5 and Figure 6 for qualitative evaluation. The corresponding denoised images by CCADN, MCCAN without local cycles, MCCAN without global cycles, and MCCAN are shown in Figure 5(b) through (e) and Figure 6(b) through (e), respectively. From the figures, we can see that CCADN can successfully reduce noise in the original images. MCCAN without local cycles completely fails to produce reasonable results. A close examination of the images reveals that interestingly the background and the substances are approximately swapped compared with the original images. This is because the high-level features of content distribution are still kept even with such swap, and the discriminator cannot identify the generated image as "fake" because of the structure diversity in the training dataset. This aligns with our discussion on the importance of local cycles in Section 2. We can make a closer comparison on the area indicated by yellow arrows in Figure 5 and Figure 6. We can observe that compared with the original images and CCADN, only MCCAN can successfully remove the tiny spot indicated by a yellow arrow in Figure 5. In addition, MCCAN and MCCAN without global cycles can remove the small hole in Figure 6, which should not exist in the vessel. However, MCCAN without global cycles can successfully denoise the image and achieves similar quality compared with CCADN. This is expected, as MCCAN without global cycles is essentially formed by two cascaded CCADNs. Finally, although MCCAN without local cycles and the complete MCCAN have competitive visual performance with each other, the complete MCCAN has relatively smaller noise (less spots and more smooth boundary) visually.

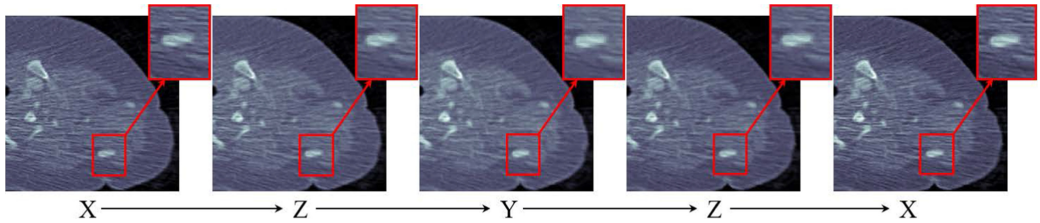

Fig. 7. An image transformed through the $X \rightarrow Z \rightarrow Y \rightarrow Z \rightarrow X$ cycle in Figure 3. The noise level decreases along $X \rightarrow Z \rightarrow Y$ and increases along $Y \rightarrow Z \rightarrow X$, which conforms to our design.

Table 3. Mean and SD of the Selected Areas in Figure 5

Method	Original		CCADN [40]		MCCAN w/o Local Cycles		MCCAN w/o Global Cycles		MCCAN	
	Mean	SD	Mean	SD	Mean	SD	Mean	SD	Mean	SD
Area #1	1,942.3	118.0	1801.2	100.2	30.9	45.2	1,747.7	92.6	1,712.8	89.8
Area #2	903.3	60.0	928.8	47.1	215.0	60.9	932.1	46.0	940.5	40.8
Area #3	913.6	58.1	938.2	46.0	96.7	41.2	943.5	46.4	938.0	41.3
Area #4	1,944.0	132.6	1,821.5	103.8	43.8	55.6	1,762.2	97.3	1,723.5	94.5
Area #5	903.2	53.8	930.7	42.0	255.0	70.7	934.0	43.4	942.2	36.6

Table 4. Mean and SD of the Selected Areas in Figure 6

Method	Original		CCADN [40]		MCCAN w/o Local Cycles		MCCAN w/o Global Cycles		MCCAN	
	Mean	SD	Mean	SD	Mean	SD	Mean	SD	Mean	SD
Area #1	1,067.2	24.8	1,057.75	20.4	87.2	12.1	1,058.5	20.58	1,061.9	19.53
Area #2	1,568.4	62.4	1,498.4	60.6	47.9	22.6	1,504.0	59.1	1,547.9	54.8
Area #3	1,052.9	34.4	1,044.1	27.9	56.4	12.3	1,044.8	28.0	1,047.0	24.2
Area #4	906.6	43.2	942.6	37.7	120.1	25.7	930.7	33.4	897.1	30.9
Area #5	1,082.2	66.11	1,191.3	51.8	254.3	43.0	1,165.5	50.7	1,147.3	48.8
Area #6	1,233.0	76.9	1,398.2	65.4	176.0	56.3	1,364.6	64.4	1,367.7	63.6
Area #7	992.5	230.4	968.9	190.0	340.2	67.2	1,010.3	188.8	995.8	178.3

To further illustrate the efficacy of the MCCAN structure, Figure 7 shows how an image is transformed along a global cycle (the path $X \rightarrow Z \rightarrow Y \rightarrow Z \rightarrow X$). From the figure, we can see that $X \rightarrow Z \rightarrow Y$ is an effective two-step denoising process, whereas $Y \rightarrow Z \rightarrow X$ incrementally adds noise back.

4.3.3 Quantitative Evaluation. The quantitative results are shown in Table 3 and Table 4. CCADN can reduce the SD in the 12 areas by 15%, 21%, 21%, 22%, 22%, 18%, 3%, 19%, 13%, 22%, 15%, and 18%, respectively, with resulting mean values close to those of the original images. Although MCCAN without local cycles achieves the smallest SD in Areas 1, 3 and 4, it leads to large mean deviation from the original images, which corresponds to the structure loss in Figure 5(c). MCCAN without global cycles has performance similar to CCADN, with mean values close to original and SD reduction by 22%, 23%, 20%, 27%, 19%, 17%, 5%, 19%, 23%, 23%, 16%, and 18%,

respectively. Finally, the complete MCCAN behaves the best among all of the methods. With mean values close to original, the SDs are decreased by 24%, 32%, 29%, 29%, 32%, 21%, 12%, 30%, 28%, 26%, 17%, and 23% from the original CT images, respectively.

5 CONCLUSION

In this article, we propose MCCAN for edge denoising of CT images. MCCAN builds intermediate domains and enforces both local and global cycle-consistency. The global cycle-consistency couples all generators together to model the whole denoising process, whereas the local cycle-consistency imposes effective supervision on the denoising process between adjacent domains. Experiments show that both local and global cycle-consistency are important for the success of MCCAN, and it outperforms the state-of-the-art competitor with slightly less resource consumption. Our code is publicly available. Considering the practical usage, the computation complexity and the denoising performance still need further improvement, and our future work will focus on optimizing the denoising performance while reducing the computation operations at the same time. In future work, we will try to apply MCCAN to other medical images, such as magnetic resonance imaging and ultrasound, and explore the cycle design theoretically.

REFERENCES

[1] Asha Anoosheh, Eirikur Agustsson, Radu Timofte, and Luc Van Gool. 2018. ComboGAN: Unrestrained scalability for image domain translation. In *Proceedings of the IEEE Conference on Computer Vision and Pattern Recognition Workshops*. 783–790.

[2] I. Arapakis, E. Efstathopoulos, V. Tsitsia, S. Kordolaimi, N. Economopoulos, S. Argentos, A. Ploussi, and E. Alexopoulou. 2014. Using "iDose4" iterative reconstruction algorithm in adults' chest–abdomen–pelvis CT examinations: Effect on image quality in relation to patient radiation exposure. *British Journal of Radiology* 87, 1036 (2014).

[3] Hu Chen, Yi Zhang, Weihua Zhang, Peixi Liao, Ke Li, Jiliu Zhou, and Ge Wang. 2017. Low-dose CT denoising with convolutional neural network. In *Proceedings of the 2017 IEEE 14th International Symposium on Biomedical Imaging (ISBI'17)*. IEEE, Los Alamitos, CA, 143–146.

[4] Yunjey Choi, Minje Choi, Munyoung Kim, Jung-Woo Ha, Sunghun Kim, and Jaegul Choo. 2017. StarGAN: Unified generative adversarial networks for multi-domain image-to-image translation. arXiv:1711.09020.

[5] Leon A. Gatys, Alexander S. Ecker, and Matthias Bethge. 2016. Image style transfer using convolutional neural networks. In *Proceedings of the IEEE Conference on Computer Vision and Pattern Recognition*. 2414–2423.

[6] Michael Green, Edith M. Marom, Eli Konen, Nahum Kiryati, and Arnaldo Mayer. 2018. Learning real noise for ultra-low dose lung CT denoising. In *Proceedings of the International Workshop on Patch-Based Techniques in Medical Imaging*. 3–11.

[7] Kaiming He, Xiangyu Zhang, Shaoqing Ren, and Jian Sun. 2016. Deep residual learning for image recognition. In *Proceedings of the IEEE Conference on Computer Vision and Pattern Recognition*. 770–778.

[8] Jason B. Hobbs, Noah Goldstein, Kimberly E. Lind, Deirdre Elder, Gerald D. Dodd III, and James P. Borgstede. 2018. Physician knowledge of radiation exposure and risk in medical imaging. *Journal of the American College of Radiology* 15, 1 (2018), 34–43.

[9] Phillip Isola, Jun-Yan Zhu, Tinghui Zhou, and Alexei A. Efros. 2017. Image-to-image translation with conditional adversarial networks. arXiv:1611.07004.

[10] Justin Johnson, Alexandre Alahi, and Li Fei-Fei. 2016. Perceptual losses for real-time style transfer and super-resolution. In *Proceedings of the European Conference on Computer Vision*. 694–711.

[11] Eunhee Kang, Hyun Jung Koo, Dong Hyun Yang, Joon Bum Seo, and Jong Chul Ye. 2018. Cycle consistent adversarial denoising network for multiphase coronary CT angiography. arXiv:1806.09748.

[12] Boaz Karmazyn, Donald P. Frush, Kimberly E. Applegate, Charles Maxfield, Mervyn D. Cohen, and Robert P. Jones. 2009. CT with a computer-simulated dose reduction technique for detection of pediatric nephroureterolithiasis: Comparison of standard and reduced radiation doses. *American Journal of Roentgenology* 192, 1 (2009), 143–149.

[13] Taeksoo Kim, Moonsu Cha, Hyunsoo Kim, Jung Kwon Lee, and Jiwon Kim. 2017. Learning to discover cross-domain relations with generative adversarial networks. In *Proceedings of the International Conference on Machine Learning*. 1857–1865.

[14] Zhoubo Li, Lifeng Yu, Joshua D. Trzasko, David S. Lake, Daniel J. Blezek, Joel G. Fletcher, Cynthia H. McCollough, and Armando Manduca. 2014. Adaptive nonlocal means filtering based on local noise level for CT denoising. *Medical Physics* 41, 1 (2014), 011908.

[15] Jin Liu, Jianhua Ma, Yi Zhang, Yang Chen, Jian Yang, Huazhong Shu, Limin Luo, et al. 2017. Discriminative feature representation to improve projection data inconsistency for low dose CT imaging. *IEEE Transactions on Medical Imaging* 36, 12 (2017), 2499–2509.

[16] Jiaying Liu, Wenhan Yang, Shuai Yang, and Zongming Guo. 2018. Erase or fill? Deep joint recurrent rain removal and reconstruction in videos. In *Proceedings of the IEEE Conference on Computer Vision and Pattern Recognition*. 3233–3242.

[17] Ming-Yu Liu and Oncel Tuzel. 2016. Coupled generative adversarial networks. In *Advances in Neural Information Processing Systems*. 469–477.

[18] Zihao Liu, Xiaowei Xu, Tao Liu, Qi Liu, Yanzhi Wang, Yiyu Shi, Wujie Wen, Meiping Huang, Haiyun Yuan, and Jian Zhuang. 2019. Machine vision guided 3D medical image compression for efficient transmission and accurate segmentation in the clouds. In *Proceedings of the IEEE/CVF Conference on Computer Vision and Pattern Recognition*. 12687–12696.

[19] Armando Manduca, Lifeng Yu, Joshua D. Trzasko, Natalia Khaylova, James M. Kofler, Cynthia M. McCollough, and Joel G. Fletcher. 2009. Projection space denoising with bilateral filtering and CT noise modeling for dose reduction in CT. *Medical Physics* 36, 11 (2009), 4911–4919.

[20] William W. Mayo-Smith, Amy K. Hara, Mahadevappa Mahesh, Dushyant V. Sahani, and William Pavlicek. 2014. How I do it: Managing radiation dose in CT. *Radiology* 273, 3 (2014), 657–672.

[21] Mehdi Mirza and Simon Osindero. 2014. Conditional generative adversarial nets. arXiv:1411.1784.

[22] John Nuyts, Bruno De Man, Patrick Dupont, Michel Defrise, Paul Suetens, and Luc Mortelmans. 1998. Iterative reconstruction for helical CT: A simulation study. *Physics in Medicine & Biology* 43, 4 (1998), 729.

[23] Rui Qian, Robby T. Tan, Wenhan Yang, Jiajun Su, and Jiaying Liu. 2018. Attentive generative adversarial network for raindrop removal from a single image. In *Proceedings of the IEEE Conference on Computer Vision and Pattern Recognition*. 2482–2491.

[24] Hongming Shan, Yi Zhang, Qingsong Yang, Uwe Kruger, Mannudeep K. Kalra, Ling Sun, Wenxiang Cong, and Ge Wang. 2018. 3-D convolutional encoder-decoder network for low-dose CT via transfer learning from a 2-D trained network. *IEEE Transactions on Medical Imaging* 37, 6 (2018), 1522–1534.

[25] Aaron Sodickson, Pieter F. Baeyens, Katherine P. Andriole, Luciano M. Prevedello, Richard D. Nawfel, Richard Hanson, and Ramin Khorasani. 2009. Recurrent CT, cumulative radiation exposure, and associated radiation-induced cancer risks from CT of adults. *Radiology* 251, 1 (2009), 175–184.

[26] Jifeng Wang, Xiang Li, and Jian Yang. 2018. Stacked conditional generative adversarial networks for jointly learning shadow detection and shadow removal. In *Proceedings of the IEEE Conference on Computer Vision and Pattern Recognition*. 1788–1797.

[27] Tianchen Wang, Xiaowei Xu, Jinjun Xiong, Qianjun Jia, Haiyun Yuan, Meiping Huang, Jian Zhuang, and Yiyu Shi. 2020. ICA-UNet: ICA inspired statistical UNet for real-time 3D cardiac cine MRI segmentation. In *Proceedings of the International Conference on Medical Image Computing and Computer-Assisted Intervention*. 447–457.

[28] Jelmer M. Wolterink, Tim Leiner, Max A. Viergever, and Ivana Išgum. 2017. Generative adversarial networks for noise reduction in low-dose CT. *IEEE Transactions on Medical Imaging* 36, 12 (2017), 2536–2545.

[29] Fang Xu and Klaus Mueller. 2007. Real-time 3D computed tomographic reconstruction using commodity graphics hardware. *Physics in Medicine & Biology* 52, 12 (2007), 3405.

[30] Xiaowei Xu, Yukun Ding, Sharon Xiaobo Hu, Michael Niemier, Jason Cong, Yu Hu, and Yiyu Shi. 2018. Scaling for edge inference of deep neural networks. *Nature Electronics* 1, 4 (2018), 216–222.

[31] Xiaowei Xu, Qing Lu, Lin Yang, Sharon Hu, Danny Chen, Yu Hu, and Yiyu Shi. 2018. Quantization of fully convolutional networks for accurate biomedical image segmentation. In *Proceedings of the IEEE Conference on Computer Vision and Pattern Recognition*. 8300–8308.

[32] Xiaowei Xu, Tianchen Wang, Yiyu Shi, Haiyun Yuan, Qianjun Jia, Meiping Huang, and Jian Zhuang. 2019. Whole heart and great vessel segmentation in congenital heart disease using deep neural networks and graph matching. In *Proceedings of the International Conference on Medical Image Computing and Computer-Assisted Intervention*. 477–485.

[33] Xiaowei Xu, Tianchen Wang, Jian Zhuang, Haiyun Yuan, Meiping Huang, Jianzheng Cen, Qianjun Jia, Yuhao Dong, and Yiyu Shi. 2020. ImageCHD: A 3D computed tomography image dataset for classification of congenital heart disease. In *Proceedings of the International Conference on Medical Image Computing and Computer-Assisted Intervention*. 77–87.

[34] Qingsong Yang, Pingkun Yan, Yanbo Zhang, Hengyong Yu, Yongyi Shi, Xuanqin Mou, Mannudeep K. Kalra, Yi Zhang, Ling Sun, and Ge Wang. 2018. Low-dose CT image denoising using a generative adversarial network with Wasserstein distance and perceptual loss. *IEEE Transactions on Medical Imaging* 37, 6 (2018), 1348–1357.

[35] Zili Yi, Hao (Richard) Zhang, Ping Tan, and Minglun Gong. 2017. DualGAN: Unsupervised dual learning for image-to-image translation. In *Proceedings of the 2017 IEEE International Conference on Computer Vision (ICCV'17)*. 2868–2876.

[36] Chenyu You, Qingsong Yang, Lars Gjesteby, Guang Li, Shenghong Ju, Zhuiyang Zhang, Zhen Zhao, et al. 2018. Structurally-sensitive multi-scale deep neural network for low-dose CT denoising. *IEEE Access* 6 (2018), 41839–41855.

[37] Jiawei Zhang, Yuzhen Jin, Jilan Xu, Xiaowei Xu, and Yanchun Zhang. 2018. MDU-Net: Multi-scale densely connected U-Net for biomedical image segmentation. arXiv:1812.00352.
[38] Jiawei Zhang, Yanchun Zhang, and Xiaowei Xu. 2021. Pyramid U-Net for retinal vessel segmentation. arXiv:2104.02333.
[39] Jiawei Zhang, Yanchun Zhang, Shanfeng Zhu, and Xiaowei Xu. 2020. Constrained multi-scale dense connections for accurate biomedical image segmentation. In *Proceedings of the 2020 IEEE International Conference on Bioinformatics and Biomedicine (BIBM'20)*. IEEE, Los Alamitos, CA, 877–884.
[40] Jun-Yan Zhu, Taesung Park, Phillip Isola, and Alexei A. Efros. 2017. Unpaired image-to-image translation using cycle-consistent adversarial networks. arXiv:1703.10593.

Received May 2020; revised December 2020; accepted April 2021